

Article

Effects of Flexural Stiffness on Deformation Behaviour of Steel and FRP Stress-Ribbon Bridges

Algirdas Juozapaitis ¹, Giedrė Sandovič ¹, Ronaldas Jakubovskis ² and Viktor Gribniak ^{1,2,*} 

¹ Department of Steel and Composite Structures, Vilnius Gediminas Technical University, Vilnius TECH, LT-10223 Vilnius, Lithuania; Algirdas.Juozapaitis@vilniustech.lt (A.J.); Giedre.Sandovic@vilniustech.lt (G.S.)

² Laboratory of Innovative Building Structures, Vilnius TECH, LT-10223 Vilnius, Lithuania; Ronaldas.Jakubovskis@vilniustech.lt

* Correspondence: Viktor.Gribniak@vilniustech.lt; Tel.: +370-6-134-6759

Featured Application: A new structural system of the pedestrian bridge with ribbons made of flexural-stiff profiles is introduced and physically tested, proving its efficiency.

Abstract: Stress-ribbon systems develop the most flexible and slender bridges. A structural system of such elegant bridges consists of cables or ribbons and deck slabs placed to these strips to distribute the live load. Although this structural system is simple, the design of such structures is a challenging issue. Design limitations of the bridge deck slope induce considerable forces in the ribbons, which transfer the tension to massive foundations. The deformation increase under concentrated and asymmetrical loads causes another problem of stress-ribbon bridges—the kinematic component, the design object of such structures, exceeds the dead load-induced vertical displacement several times. This paper introduces a new concept of such a structural system, comprising ribbons made of flexural-stiff profiles. The proposed approach to reduce kinematic displacements is illustrated experimentally by testing two pedestrian bridge prototypes with different flexural stiffness of the steel ribbons. Numerical models calibrated using the test results are used for the parametric analysis of the flexural stiffness effect on the deformation behaviour of the bridge system with steel and fibre-reinforced polymer (FRP) ribbons. A practical approach to the choice of the efficient flexural stiffness of the ribbon-profiles is also proposed.

Keywords: stress-ribbon bridge; kinematic displacement; flexural stiffness; physical tests; steel ribbons; fibre-reinforced polymer; numerical modelling; analytical model



Citation: Juozapaitis, A.; Sandovič, G.; Jakubovskis, R.; Gribniak, V. Effects of Flexural Stiffness on Deformation Behaviour of Steel and FRP Stress-Ribbon Bridges. *Appl. Sci.* **2021**, *11*, 2585. <https://doi.org/10.3390/app11062585>

Academic Editors: Jong Wan Hu and Panagiotis G. Asteris

Received: 12 February 2021

Accepted: 11 March 2021

Published: 14 March 2021

Publisher's Note: MDPI stays neutral with regard to jurisdictional claims in published maps and institutional affiliations.



Copyright: © 2021 by the authors. Licensee MDPI, Basel, Switzerland. This article is an open access article distributed under the terms and conditions of the Creative Commons Attribution (CC BY) license (<https://creativecommons.org/licenses/by/4.0/>).

1. Introduction

The stress-ribbon layout is one of the oldest structural systems efficient for pedestrian bridges [1]. The assemblage slenderness makes such elegant structures an intrinsic part of the modern infrastructure [1–5]. A slightly sagged suspension band forms a catenary shape that looks natural and aesthetically attractive. The structural system of such bridges consists of cables and ribbons and the deck slabs placed on them. Typically, spiral strands and flexible bands made of steel are used for that purpose, though the number of fibre-reinforced polymers (FRP) application examples is continuously increasing [4,6]. The deck slabs, distributing the load to the supporting bands, often do not affect the load-bearing capacity of the bridge. Although this structural system is simple, its design is challenging. The serviceability demands limit the bridge deck slope to 8–12% [7,8], reducing the sag-to-span ratio (f/l) to the range of 0.020–0.033. Thus, large foundations are necessary to resist tremendous tension forces acting on the ribbons.

Another problem is related to the deformability of the stress-ribbon systems under concentrated and asymmetrical loads [1,5,9]—the kinematic displacement magnitude, the structural design object, can several times exceed the dead load-induced displacement component [10]. Enlarging the dead load, pre-stressing the concrete bridges, and increasing the

flexural stiffness of the structural system can solve the above problem. The self-weight increase is the simplest way to stabilise the structure [1]; however, the dead load increases the thrust force acting on the ribbons. The pre-stress technologies require specialised anchorage systems and can cause a sudden bridge failure [11,12]. Juozapaitis et al. [13] revealed that the flexural-stiff suspension systems can efficiently reduce the kinematic displacements.

This paper introduces an innovative concept of the stress-ribbon structural system with flexural-stiff ribbons. The application of hot-rolled and welded steel profiles simplifies the construction process. Furthermore, this structural system ensures the formation of lightweight decks, reducing axial forces in the ribbons. The proposed concept can be extended to the pultruded FRP profiles. However, bending stresses in the ribbons increase with increasing the flexural stiffness. Combining different materials in a composite cross-section can solve this problem, but it requires developing the connection technologies and design procedures [14–17]. Thus, the optimisation of the bridge geometry and material properties becomes a crucial issue [18,19]. Besides, conventional techniques do not apply to the design of the anisotropic material components [20].

Numerical methods could be a powerful tool for solving a broad spectrum of engineering problems [21]. Romera et al. [4] and Xiao et al. [5] investigated dynamics problems of the suspension bridges. Radnić et al. [12] and Votsis et al. [22] carried out numerical simulations of stress-ribbon and suspension bridges to optimise the ribbons' material parameters and geometry. However, a limited number of experimental works in the field do not determine the optimum flexural stiffness of the ribbons. The contributions by Bleicher et al. [23], Juozapaitis et al. [24], and Sandovic et al. [25] should be mentioned as rare examples of such experimental studies.

This study is a continuation of the researches [24,25]. It experimentally investigates the deformation behaviour of two pedestrian steel bridge prototypes: one has flexible bands typical of such structural systems and an alternative structure with the innovative flexural-stiff ribbons. Numerical models calibrated using the test results are used for the parametric analysis of the flexural stiffness effect on the deformation behaviour of the bridge system with steel and fibre-reinforced polymer (FRP) ribbons. A practical approach to the choice of the stiffness of the ribbon-profiles is also proposed.

2. Design Procedure of the Bridge with Flexural-Stiff Ribbons

The ribbons are designed to resist substantial axial forces, transferring them to massive foundations. The stress-ribbon bridge shape also has no strict limitations; in some cases, the movement requirements of special vehicles can limit the maximal slope of the bridge deck. However, the stress-ribbon bridges can undergo significant displacements, particularly from concentrated and asymmetrically distributed loads. Thus, the limitations of vertical displacements become the governing design condition [1,7,19]. The displacement increment induced by the live load (q), regarding the dead-load deformed shape, is the design criterion.

Figure 1 shows the design scheme of the stress-ribbon bridge, having an initial sag of the ribbons f_0 . The dead load g increases the vertical displacement. A parabolic curve approximately describes this deformed shape that is the onset of design calculations. In other words, a live load (q) induces additional displacement $u_q(x)$ that is the limitation object—various load distribution layouts determine the maximum vertical displacement

$$u_{q,max}(x) \leq u_{q,lim} \quad (1)$$

where $u_{q,lim}$ is the displacement limit.

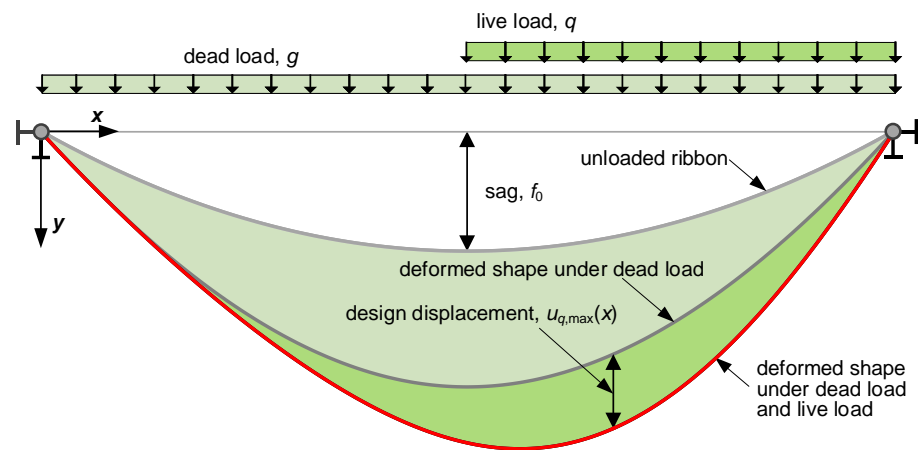


Figure 1. The design scheme of a stress-ribbon bridge.

The stress-ribbon systems are sensitive to the load q distributed over the bridge half span that often induces the maximum kinematic displacement of the bridge. The loading ratio $\gamma (= q/g)$ and the flexural stiffness of the ribbons control the kinematic displacement magnitude [1,13]. The following expression determines the functional relationship between the bridge parameters and the vertical displacement [13]:

$$u_q(x) = \Phi(\gamma, x/l, (kl)^{-1}, \Omega[kl, kx]) \leq u_{q,lim} \tag{2}$$

where l is the bridge span; the coefficient $k = \sqrt{H/EI_y}$ defines slenderness of the ribbon (H is the thrust force, EI_y is the flexural stiffness of the ribbon); the operand $\Omega[kl, kx]$ represents a combination of hyperbolic functions of the variables given in the brackets. A mathematical expression of Equation (2) depends on the structural parameters and boundary conditions of the ribbons. Juozapaitis and Norkus [26] formulated several examples of such equations for the steel ribbon, having three hinges.

The proposed approach to the choice of the efficient geometry of the ribbon cross-section, expressed in terms of the flexural stiffness, employs an iterative calculus accounting for ULS (ultimate limit state) and SLS (serviceability limit state) limitations. The following expression defines the required second moment of inertia of the ribbon subjected to an unsymmetrical load distributed over the bridge half span, using the beam analogy and satisfying condition (1):

$$I_y \geq \frac{1}{156} \cdot \frac{q_{eq}^* \cdot l_q^4}{u_{q,lim} \cdot E} \tag{3}$$

where $u_{q,lim}$ is the displacement limit; q_{eq}^* is the load uniformly distributed over the span length l_q (in this case, $l_q = l/2$), i.e., $q_{eq}^* = q/2$; E is the elasticity modulus.

The ULS limits define the condition for determining the cross-section parameters:

$$H \leq \frac{A \cdot f_d}{\beta} \tag{4}$$

where H is the thrust force; A is the cross-section area; f_d is the design strength of the material; the coefficient β is calculated, as follows:

$$\beta = 1 + \frac{e}{2 \cdot \alpha_c^2 \cdot h_c} \tag{5}$$

where α_c is the shape coefficient; h_c is the cross-section height. The eccentricity e can be approximated, using the beam analogy, as follows:

$$e \approx \frac{48 \cdot u_{q,lim} \cdot EI_y}{5 \cdot l_q^2 \cdot H} \tag{6}$$

where EI_y is the flexural stiffness of the ribbon.

The minimum required cross-section area can be obtained from condition (4), accounting for expressions (5) and (6), as follows:

$$A \geq \frac{H}{f_d} \left(1 + \frac{24 \cdot u_{q,lim} \cdot E}{5 \cdot \alpha_c^2 \cdot h_c \cdot k^2 \cdot I_q} \right) \quad (7)$$

where k is the slenderness coefficient from Equation (2). The following equation determines the required cross-section height:

$$h_c = \left\{ \left(\frac{12 \cdot u_{q,lim}}{5 \cdot l_q^2 \cdot k^2 \cdot \alpha_c^2} \right)^2 + \frac{f_d}{k^2 \cdot E \cdot \alpha_c^2} \right\}^{1/2} - \frac{12 \cdot u_{q,lim}}{5 \cdot l_q^2 \cdot k^2 \cdot \alpha_c^2} \quad (8)$$

Remarkably, the compressive stresses in ribbons increase with increasing the flexural stiffness (EI_y) because of the bending effect. That can cause stability problems of the flexural-stiff ribbons. Besides, the magnitude of compressive stresses must be limited in structural elements made from FRP [15,20,27]. For simplicity, this study assumes the following stress limitation in the ribbons:

$$\sigma \geq 0 \quad (9)$$

The above condition limits the height of the cross-section, accounting for expressions (4) and (5), as follows:

$$h_c \leq \frac{M}{2 \cdot H \cdot \alpha_c^2} \quad (10)$$

where M is the bending moment in the ribbon.

Equations (5), (7), and (8) include the shape coefficient that is calculated, as follows:

$$\alpha_c = \left(I_y / A h_c^2 \right)^{1/2} \quad (11)$$

The recurrent relationship between Equations (7), (8), and (11) forms the iteration process. At the first iteration, an approximate value of the coefficient α_c is assumed. For this purpose, Equation (11) was applied to the profiles listed in the European Norm for Structural Sections in Steel (EN 10365). Table 1 summarises the estimated values of the coefficient α_c for the first iteration. The iterative process is repeated, beginning Equations (8) and (7) and using the coefficient α_c calculated by the Equation (11) at the previous iteration, as long as the difference between the assumed (beginning the iteration) and newly obtained α_c value remains significant.

Table 1. Approximated values of the shape coefficient α_c .

Cross-Section Type (EN 10365)	Height, mm	Estimated Coefficient
IPE-beam	160–600	0.410–0.405
HE-beam	200–900	0.430–0.405
Square hollow section	80–400	0.381–0.393
Round hollow section	88.9–1219	0.337–0.348

3. Experimental Program

Two pedestrian steel bridge prototypes of a 5 m span were built up and tested in the Laboratory of Building Structures and Geotechnics at Vilnius Gediminas Technical University (Vilnius Tech). The prototype ribbons had a pinned connection to rigid supports fixed to the strong floor. The axial stiffness of the steel ribbons was the same in both prototypes ($EA = 96$ MN, where A is the cross-section area; $E \approx 208$ GPa is the elasticity modulus), but the flexural stiffness was significantly different. In the first model, the ribbons

were designed as flexible bands with a small second moment of inertia ($I_y = 0.14 \text{ cm}^4$) and the initial sag $f_0 = 135 \text{ mm}$. The innovative ribbon-profiles of the second model were designed by using the methodology described in Section 2 without limitation of the stress in the ribbons, i.e., disregarding conditions (9) and (10), obtaining the inertia moment $I_y = 63.7 \text{ cm}^4$ and initial sag $f_0 = 75 \text{ mm}$. In this manuscript, the notations *Model-1* and *Model-2* define the prototypes with flexible bands and flexural-stiff ribbon-profiles. Figure 2 shows the corresponding bridge schemes.

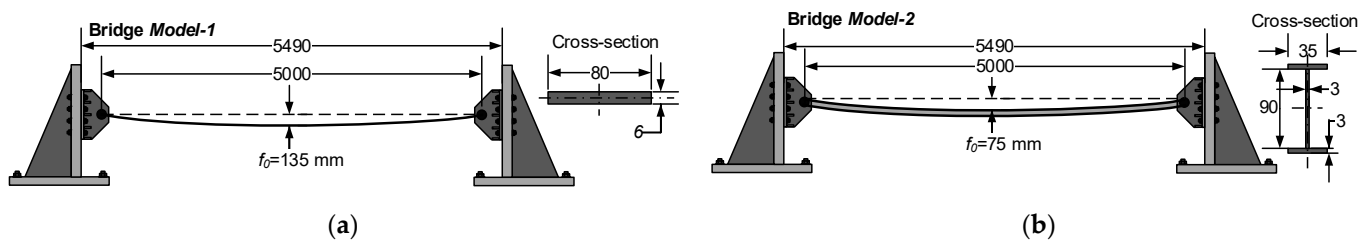


Figure 2. Geometry characteristics of the prototypes with different flexural stiffness of stress-ribbons: (a) the bridge with flexible bands; (b) the bridge with flexural-stiff ribbon-profiles.

3.1. Loading Procedure

Three loading layouts are considered: one symmetrical and two asymmetrical (with different ratio between the live load, q , and the dead load, g)—*Model-1* and *Model-2* were subjected to the same loading schemes. The prototypes were loaded incrementally using iron weights. Figures 3 and 4 show the loading schemes and typical arrangements of the weights corresponding to symmetrical and asymmetrical loading scenarios. The load held constant for two minutes after each loading step to stabilise the vertical displacement of the bridge systems. The increments of the symmetrical load are the following. A timber bridge deck was constructed over the steel ribbons inducing the 0.077 kN/m load at the first step. At the further increments, the iron weights ($\approx 24 \text{ kg}$ each) were distributed uniformly over the timber deck resulting in approximately 0.31 kN/m load. The final (seventh) increment induced a 2.22 kN/m load.

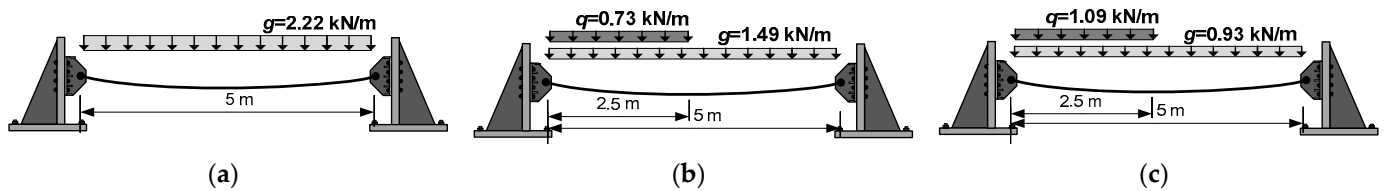


Figure 3. The bridge prototypes' loading schemes: (a) symmetrical load; (b) asymmetrical load ($q/g = 0.49$); (c) asymmetrical load ($q/g = 1.17$).

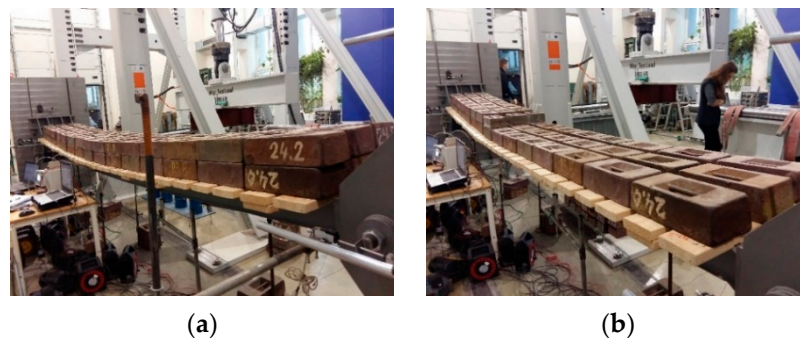


Figure 4. Typical loading layouts: (a) symmetrical load situation; (b) asymmetrical load situation.

The asymmetrical loads were applied with the ratio q/g equal to 0.49 and 1.17. In all scenarios, the dead load, g , was distributed over the bridge span in the same manner as in the symmetrical loading case (Figure 3). For the ratio $q/g = 0.49$, the first five loading increments induced the dead load $g = 1.49$ kN/m. The additional live load (q) applied in two steps has induced 0.73 kN/m distributed over the bridge half span. Analogously, the ratio $q/g = 1.17$ generated in three loading steps to achieve the target load g and three successive increments to reach the necessary magnitude of the load q . The corresponding load components are the following: $g = 0.93$ kN/m and $q = 1.09$ kN/m.

Deformations of the stress-ribbons were measured using the 20 mm strain gauges. Vertical displacements of the ribbons and horizontal movements of the supports were monitored using linear variable displacement transducers (LVDT) with a 0.01 mm accuracy. Figure 5 shows the monitoring scheme. In *Model-1* (Figure 5a), vertical displacements were recorded at the mid-span (LVDT I_3, I_4, I_9 , and I_{10}) and quarters of the span (LVDT I_2, I_8, I_5 , and I_{11}), whereas the LVDT $I_{12h}, I_{16h}, I_{17h}$, and I_{19h} monitored the horizontal movements of the supports. Deformations of the top and bottom surfaces of the steel bands were estimated at the location of the LVDT devices using the strain gauges T_7, T_8, T_{13} , and T_{14} (located at the mid-span) and two sets of the indicators (T_3, T_4, T_5, T_6 and $T_9, T_{10}, T_{15}, T_{16}$) placed at quarters of the span. *Model-2* had a similar monitoring devices' distribution scheme (Figure 5b): the LVDT I_3 and I_8 were put at the mid-span; two sets of LVDT (I_2, I_7 and I_4, I_9) were located at the span quarters. Four LVDT ($I_{11h}, I_{12h}; I_{16h}$, and I_{17h}) monitored the supports' horizontal movements. Deformations of the top and bottom surfaces of the ribbons were measured at the mid-span (using the gauges T_{17}, T_{18}, T_{10} , and T_{12}) and the span quarters (strain gauges T_3, T_4, T_7, T_9 and $T_{19}, T_{20}, T_{13}, T_{14}$).

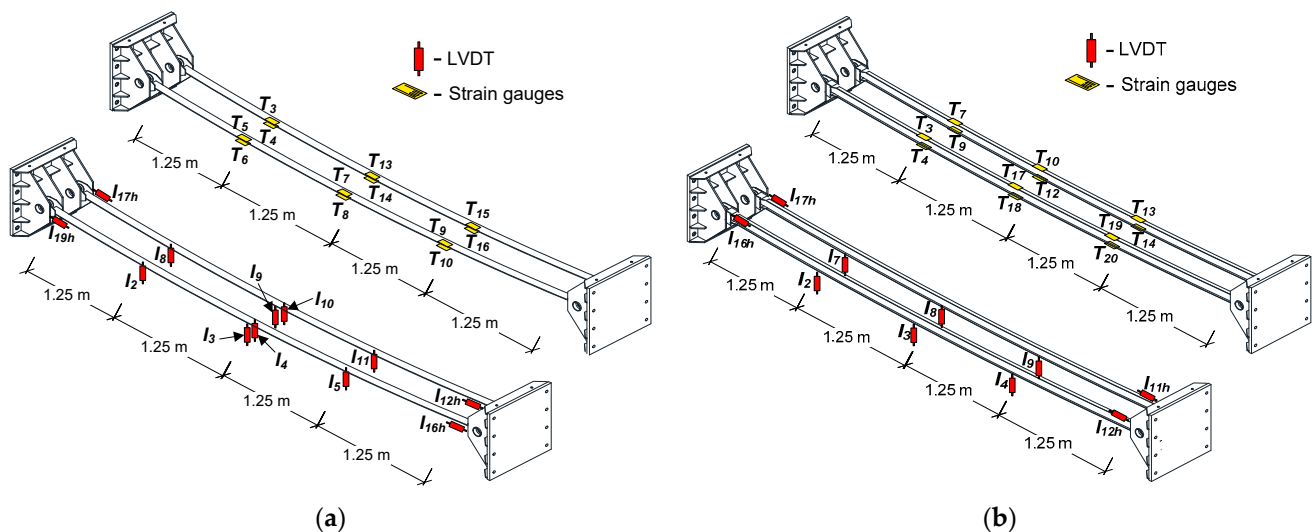


Figure 5. The monitoring devices' layout: (a) prototype with flexible bands (*Model-1*); (b) prototype with flexural-stiff ribbon-profiles (*Model-2*).

3.2. Test Results

Figures 6 and 7 show the loading results of *Model-1* and *Model-2*, respectively. The schemes include vertical and horizontal displacements of the ribbons and the estimated stresses at the ribbons' surface. These results are not suitable to compare the deformation behaviour of the prototypes because of the difference in the initial ribbon sag (f_0) of these bridges. The physical tests aimed to gather experimental data for verifying numerical models described in the next section of this manuscript.

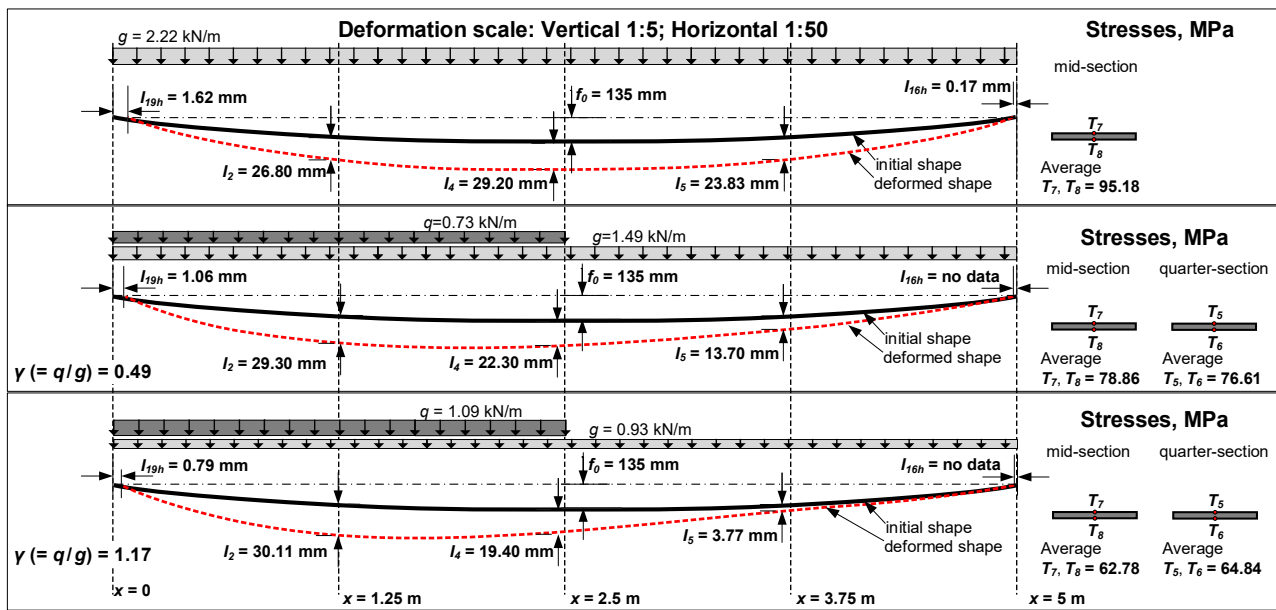


Figure 6. Monitoring results of the bridge Model-1.

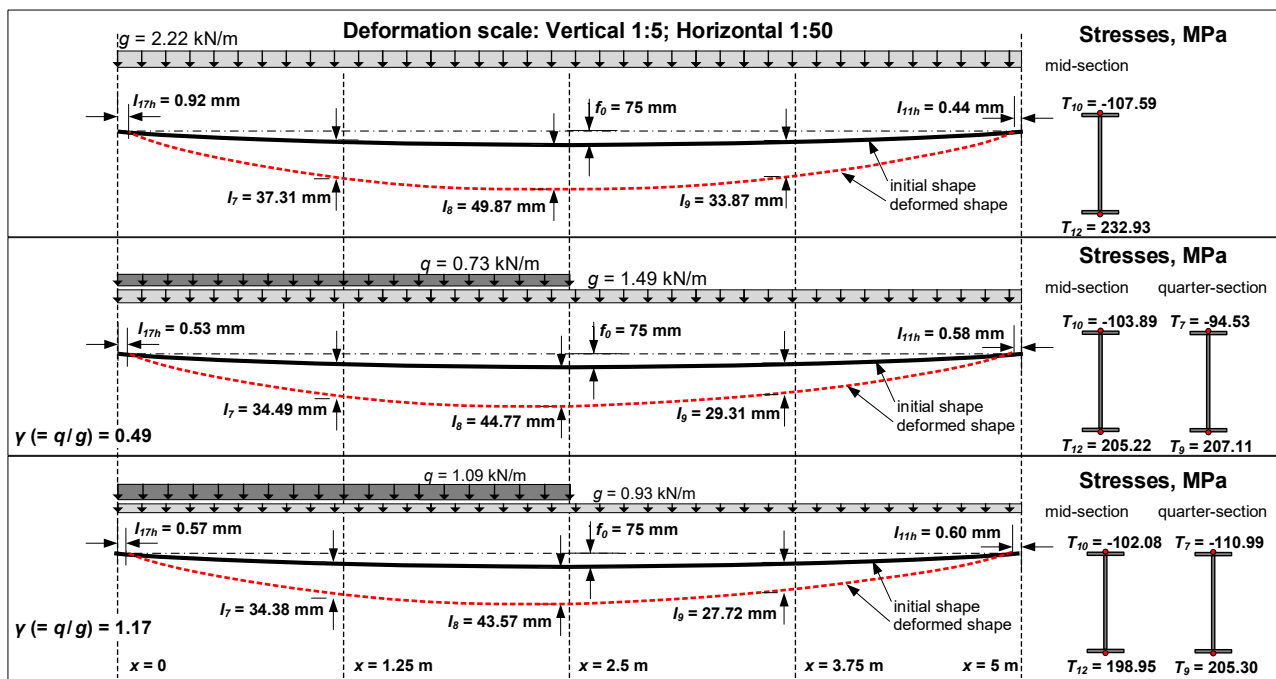


Figure 7. Monitoring results of the bridge Model-2.

However, the deformation analysis of the bridge systems reveals a beneficial feature of the model with flexural-stiff ribbon-profiles. The deformation response of the prototype with flexible bands (Figure 6) is vulnerable for asymmetrical load distribution: the maximum vertical displacement (31.1 mm) situated in the loaded quarter; a camber tends to form in the unloaded part. Model-2 (Figure 7) does not demonstrate this unfavourable tendency. The octuple difference exists between the vertical displacements measured in Model-1 span quarters under asymmetrical loading with $\gamma = 1.17$. On the contrary, this loading case induces only a 1.2 times difference between the displacements of Model-2 span quarters.

The maximum stresses observed in the ribbons of Model-2 exceeded the values estimated in Model-1 (Figures 6 and 7) due to the bending effect. The strain-gauge readings

define the stresses under the assumption of the steel ribbons' elastic deformation behaviour (the experimentally determined elasticity modulus of the steel $E_s = 208$ GPa).

4. Numerical Modelling

Numerical models were developed to analyse the flexural stiffness effect of the ribbons on the deformation behaviour of the suspension bridges. The analysis employs a finite element (FE) software ATENA. The deformation problem is solved in the 3D formulation using the Newton–Raphson iteration procedure [28].

The loading conditions include the dead load (g) distributed over the bridge span (l) and the live load (q) positioned either over the entire or half of the span. At the first stage, the permanent action is simulated. After that, the model is subjected to the live load. Both load components are applied incrementally (in five steps). Two analyses are carried out, investigating the deformation behaviour of the ribbons.

At the first analysis stage, the numerical models' adequacy is verified using the test results presented in Section 3. Two FE models are considered. One model corresponds to the bridge with flexible bands (*Model-1*); another represents the bridge with flexural-stiff ribbon-profiles (*Model-2*). As shown in Figures 6 and 7, a horizontal movement is characteristic of the supports. Springs are introduced in the numerical models to represent the support movements.

An inverse analysis was used to determine the spring stiffness corresponding to the measured horizontal displacements of the supports and the estimated thrust forces. The readings of the strain gauges T_i (Figure 5) determined the thrust forces under the assumption of elastic behaviour of the steel ribbons ($E_s = 208$ GPa). The horizontal spring stiffness was selected to predict the support movement similar to the observed during the symmetrical loading test ($g = 2.22$ kN/m). The resultant stiffness is equal to 22 kN/mm. Both models assume the same stiffness of the springs.

At the second simulation stage, a parametric analysis is performed to identify the efficient combination of the ribbons' cross-section parameters. A balance between stresses in flexural-stiff ribbon-profiles and vertical displacement gradient was the optimisation criterion—three numerical models with different flexural stiffness of the stress-ribbons are built up.

4.1. The Numerical Models' Verification

Two FE models of the bridge prototypes described in Section 3 are built up; the FE models and the prototypes have the same notation. Figure 8 shows the FE models and boundary conditions. Non-linear isoparametric shell-brick elements with nine integration points in the shell plane are used. The 3D brick elements have 20 nodes and a layered structure [29]; six internal layers are distributed in the FE shell plane. Figure 9 shows the layered FE structure. The linear-elastic isotropic material model of the steel is used for the FE analysis, assuming the elasticity modulus $E = 208$ GPa (experimental value) and Poisson's ratio $\nu = 0.30$.

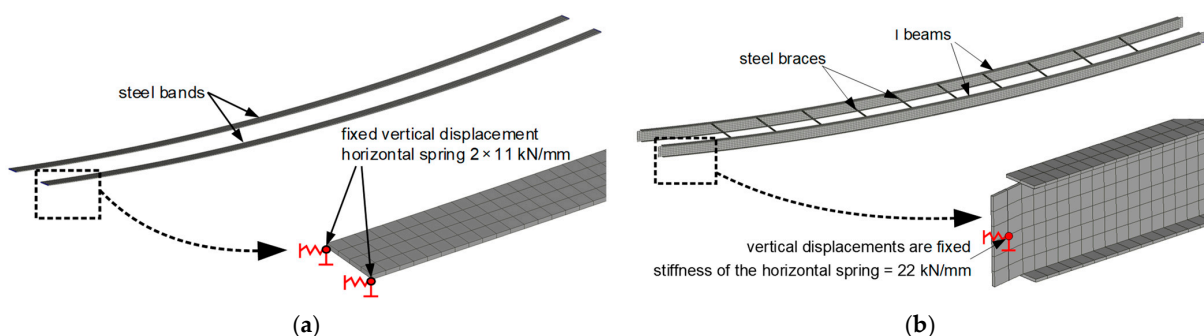


Figure 8. The bridge prototypes' FE models: (a) model with flexible bands (*Model-1*); (b) model with flexural-stiff ribbon-profiles (*Model-2*).

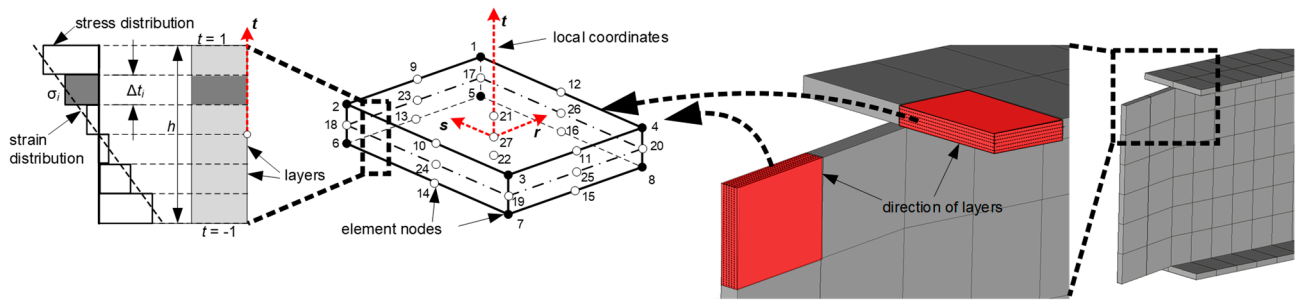


Figure 9. Shell-brick finite element and corresponding layered model.

A uniaxial deformation state is characteristic of *Model-1*. Therefore, the 20×20 mm FE mesh size is applied. The total number of finite elements in the model is 2000. However, the reference [29] recommends at least four finite elements in the bending plane to simulate the bending effects. Thus, the 18×18 mm FE mesh size is used for *Model-2*. Six elements compose the vertical wall of the section (Figure 9). The same element size is used in the flanges. Steel braces connect the flexural-stiff ribbons, preventing out-of-plane displacements of the structure. The same system was used in the corresponding bridge prototype (Section 3). The total number of finite elements in *Model-2* is 14,702.

Table 2 compares the numerical predictions and test results. The readings of the strain gauges T_i (Figure 5) determine the thrust forces under the assumption of elastic behaviour of the steel ribbons ($E_s = 208$ GPa). A high confidence level of the deformation predictions is evident: the prediction error does not exceed 7%. The disagreement can result from a relatively coarse FE model discretisation and the geometry inaccuracies of the physical prototypes. The actual difference between the initial sag (f_0) of two ribbons of *Model-2* was equal to 8.7 mm, whereas the FE model assumes the average sag value. The acceptable adequacy of the numerical predictions enables applying the FE methodology to analyse the ribbon geometry effect on resisting the kinematic displacements.

Table 2. Test and numerical results: maximum vertical displacements (u_{max}) and thrust forces (H).

Source	<i>Model-1</i>				<i>Model-2</i>			
	Symmetrical Load		Asymmetrical Load ($q/g = 0.49$)		Symmetrical Load		Asymmetrical Load ($q/g = 0.49$)	
	u_{max} , mm	H , kN	u_{max} , mm	H , kN	u_{max} , mm	H , kN	u_{max} , mm	H , kN
Test	29.2	36.0	29.3	29.5	49.9	41.3	44.8	30.2
Finite element simulations	30.5	37.9	29.5	31.7	48.8	43.2	42.0	30.6
Difference	-4.5%	-5.0%	-0.7%	-6.9%	2.2%	-4.4%	6.2%	-1.3%

Figure 10 shows the modelling example of the idealised bridge prototypes. The idealisation assumes the identical initial sag ($f_0 = 135$ mm) and loading conditions ($g = 2$ kN/m + $q = 2$ kN/m) for both *Model-1* and *Model-2*. The horizontal movements of the supports are neglected to eliminate the boundary condition influence. The experimental values (Section 3) determine the remaining parameters of the numerical models. The modelling results (Figure 10) reveal two aspects.

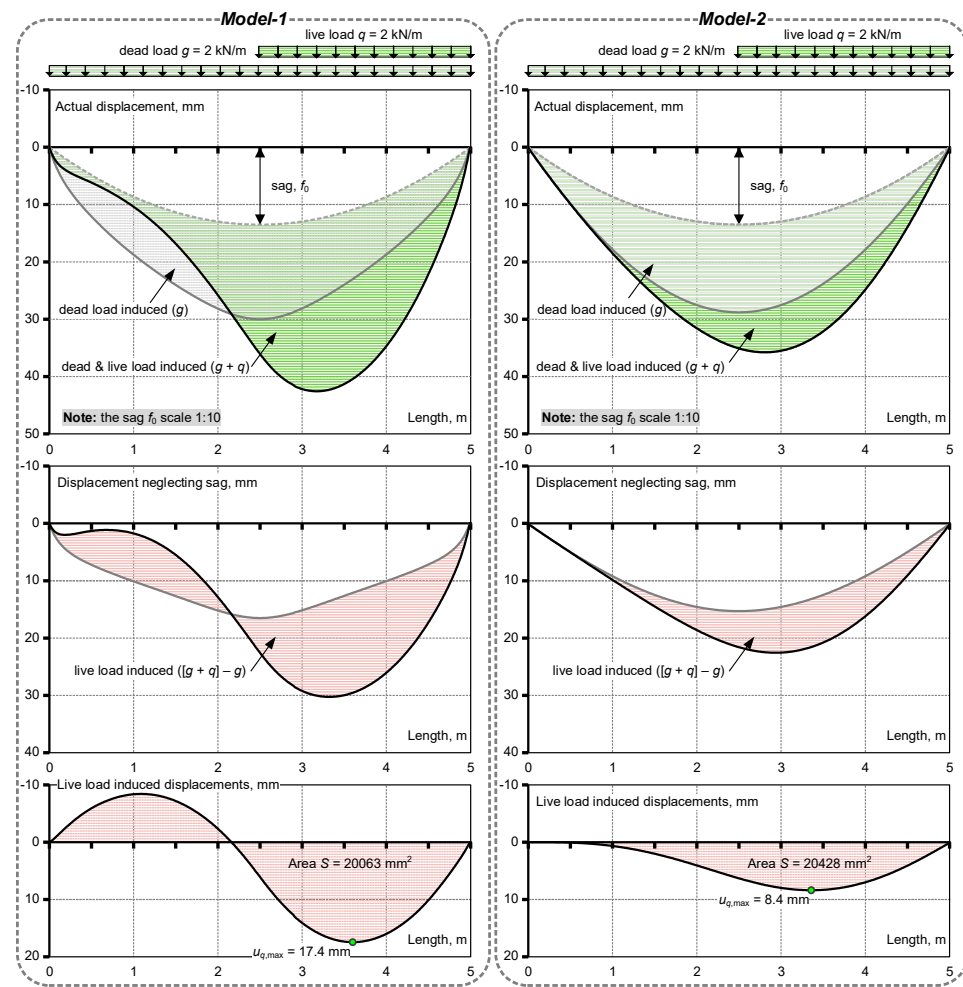


Figure 10. The bridge models’ vertical displacements.

On the one hand, the total areas (S) under the live load-induced displacement curve, determining the system’s deformation energy, are almost identical for both prototype models. That is a consequence of the loading conditions similarity. On the other hand, Figure 10 demonstrates nearly double increases in the design displacement ($u_{q,max}$) of the bridge with flexible ribbons (*Model-1*) regarding *Model-2*. The kinematic displacements also induced the substantial camber of the unloaded part of *Model-1*.

In real projects, the camber effect requires particular attention as it can cause cracking of the concrete deck and damage the joints between the deck segments. The literature review (Section 1) has suggested increasing the magnitude of the dead load (g) as a possible solution to this problem. The proposed alternative way offers the application of flexural-stiff ribbons for reducing the kinematic displacements. The next section analyses the efficiency of these two alternatives.

4.2. Parametric Analysis

The effects of flexural stiffness are investigated using three FE models with different flexural stiffness of the stress-ribbons. The horizontal movements of the supports are neglected to eliminate the influence of the boundary conditions. Figure 11 shows the considered cross-sections. The cross-section area, the material parameters, and FE type remain the same as in the previous section.

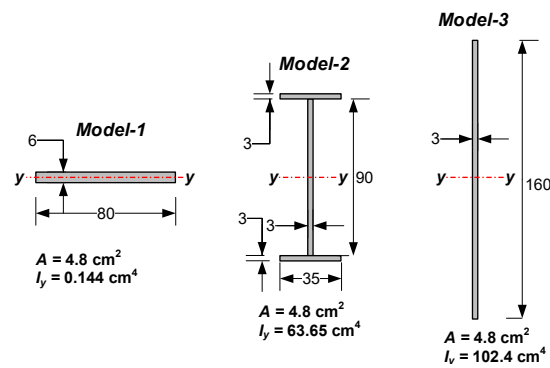


Figure 11. The ribbons’ cross-sections assumed for the parametric analysis.

The bridge sag extent, altering the magnitude of the thrust force (H), affects the choice of the cross-section parameters by the iterative procedure described in Section 2. In this section, the initial sag of *Model-2* was increased to 135 mm for illustrating the above statement by changing the compressive stresses in the ribbons. The same sag f_0 is used in all FE models considered in this section for comparison purposes.

An additional *Model-3* is investigated as a hypothetical case, representing a maximal flexural stiffness of the ribbon, though the cross-section area A does not change (Figure 11). In reality, this cross-section layout is impossible due to the low lateral-torsional buckling resistance of such a slender element. The modelling of the band half with symmetry condition along the longitudinal surface (Figure 12) ensures the buckling stability of *Model-3*.

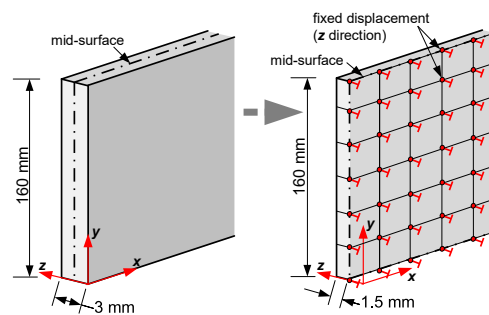


Figure 12. Symmetry conditions applied in the bridge *Model-3*.

Since the stress-ribbon bridges are susceptible to asymmetric loading conditions, the numerical analysis focuses on the deformation behaviour of the bridge models under the asymmetrical loading conditions. In the same manner as Section 4.1, the FE analyses employ the linear-elastic material model of steel, assuming the elasticity modulus $E = 208$ GPa and Poisson’s ratio $\nu = 0.30$.

The design displacement ($u_{q,max}$) induced by the live load is used for the analysis, as shown in Figure 10. The load situation of two alternative models (*Model-1* and *Model-3*) are optimised regarding the deformation response of *Model-2*. The similarity of the displacements $u_{q,max}$ of the models is the optimisation condition. This process assumes the constant design load q and alters the dead load component to satisfy the optimisation criterion (i.e., $u_{q,max} = \text{const}$).

The reference *Model-2* is subjected to the dead load $g = 2$ kN/m combined with various live load components ($q = 2$ kN/m, 3 kN/m, and 4 kN/m) applied to the bridge half span, as shown in Figures 3 and 10. The vertical displacement due to the live load (u_q) is estimated by subtracting the dead load-induced displacement component (u_g) from the total displacement predicted by the model (u_{tot}). The magnitude of the dead load applied to *Model-1* and *Model-3* is tailored iteratively to ensure the same displacement $u_{q,max}$ as the reference *Model-2*. Table 3 presents the calculation results in terms of the maximum vertical

Table 3. Design results of alternative bridge models: vertical displacement components, extremum stresses, and thrust force.

Bridge Model	$q = 2 \text{ kN/m}$						$q = 3 \text{ kN/m}$						$q = 4 \text{ kN/m}$					
	g_r kN/m	u_{tot} mm	u_q mm	σ_{min} MPa	σ_{max} MPa	H_r kN	g_r kN/m	u_{tot} mm	u_q mm	σ_{min} MPa	σ_{max} MPa	H_r kN	g_r kN/m	u_{tot} mm	u_q mm	σ_{min} MPa	σ_{max} MPa	H_r kN
Model-1	8.9	62.0	8.4	318	351	155.3	8.6	63.6	12.2	323	357	157.9	8.6	66.4	15.6	333	372	164.5
Model-2	2.0	22.6	8.4	7	221	54.2	2.0	26.3	12.2	-3	265	62.3	2.0	29.4	15.6	-14	308	70.3
Model-3	0.4	11.3	8.4	-50	154	12.6	0.4	15.1	12.2	-73	212	16.8	0.6	19.5	15.6	-92	276	22.2
Model-4	2.0	39.6	12.3	-4	64	44.2	2.0	45.0	18.2	-7	73	46.3	2.0	50.2	23.6	-10	84	52
Model-5	2.0	18.6	7.3	5	137	57	2.0	22.1	10.9	-6	165	65.3	2.0	24.8	13.8	-9	194	74.1

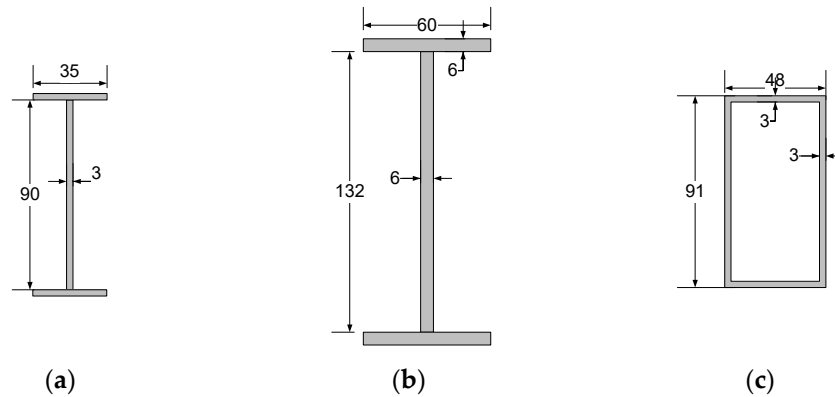


Figure 14. Alternative cross-sections: (a) steel; (b) GFRP; (c) CFRP. GFRP: glass fibre-reinforced polymer; CFRP: carbon fibre-reinforced polymer.

Table 4. Physical properties of alternative stress-ribbons.

Parameter	Steel (Model-2)	GFRP (Model-4)	CFRP (Model-5)
I_y, cm^4	63.7	458	86.5
A, cm^2	4.8	15.1	8.0
E, GPa	208	28	148
ν	0.30	0.23	0.28
EI_y, kNm^2	127.3	128.2	128.0
EA, MN	96.0	42.3	118.1
$m, \text{kg/m}$	3.77	2.72	1.52

Table 3 presents the FE simulation results of Model-4 in the grey-filled row. As expected, the minimal compressive stresses among the analysed bridge systems were induced in the GFRP ribbons. Although the flexural stiffness (EI_y) of both bridges (i.e., Model-2 and Model-4) is the same, more significant vertical displacements are characteristic of the bridge model with GFRP ribbons. It is a consequence of the high deformability of Model-4, calling for an excessive increase to the axial stiffness of GFRP ribbons because of the absence of standard profiles [30], satisfying both the axial stiffness and flexural stiffness limitations. A non-standard rectangular $127 \times 27 \text{ mm}$ (depth \times width) cross-section can be an example satisfying both the axial stiffness and the flexural stiffness conditions. The unit weight, m , of this profile is equal to 6.18 kg/m. Further reduction of the weight is impossible since it reduces the stiffness EA . That makes the GFRP profiles inefficient for this structural application.

The application of carbon fibre-reinforced polymers (CFRP) presents an acceptable solution to the above problem [4,15]. The elasticity modulus of such profiles can vary from 88 GPa to 245 GPa depending on the carbon filament content; the tensile strength can reach 2.5 GPa [31]. Thus, an alternative Model-5 has ribbons made of CFRP profiles. In this example, the CFRP elasticity modulus and strength are equal to 148 GPa and 1.1 GPa. Figure 14c shows that the cross-section composed following the design procedure described in Section 2. The cross-section shape was changed because of the CFRP composite manufac-

turing peculiarities—the chosen closed-shape conforms to the manufacturer datasheets [31]. Table 3 presents the FE calculation results (in the grey-filled row).

The FE simulations assume the elastic behaviour of both GFRP and CFRP materials. The modelling also neglects the anisotropy of FRP composites. The predominance of tensile stresses, which are relatively low regarding the FRP strength [25], makes the assumed simplifications acceptable for the deformation analysis.

Table 4 shows that the reference steel ribbon and CFRP profile have almost identical stiffness (both axial and flexural); the predicted displacements of *Model-2* and *Model-5* are similar, as well (the bold numbers indicate the characteristic values in Table 3). However, *Model-5* has the lowest unit weight (m) among the ribbons listed in Table 4.

The above results reveal the following issues:

- The existing assortment of GFRP profiles, based on the similarity of cross-section dimensions of the polymer and steel profiles, does not ensure achieving adequate efficiency as steel counterparts in situations when equivalent axial and flexural stiffness are required in conjunction.
- CFRP profiles are applicable as flexural-stiff stress-ribbons. The development of such structural systems is the object of further research.

5. Conclusions

This study develops a new concept of the stress-ribbon bridge system that comprises ribbons made of flexural-stiff profiles. The proposed approach efficiency in reducing kinematic displacements was illustrated by physical tests of two steel bridge prototypes. The finite element model, verified using the test results, was used for the parametric analysis. The following conclusions are formulated:

- A more sustainable deformation behaviour is characteristic of the bridge prototype with the innovative flexural-stiff ribbons regarding the model with flexible bands of the same axial stiffness. Even under asymmetrical load distribution (unfavourable for the typical bridge systems), the proposed ribbon-profiles did not experience undesirable camber of the unloaded part of the span. At the same time, the proposed design procedure can limit unacceptable compressive stresses in the ribbons.
- An engineering methodology and design equations are proposed to choose the cross-section geometry of the flexural-stiff ribbon-profiles. It allows composing the ribbons of any materials, increasing the versatility of the stress-ribbon structural systems.
- The existing dimensioning system of GFRP profiles, based on the cross-section similarity to the steel profiles, is inefficient in situations that require the satisfaction of both the axial stiffness and the flexural stiffness limitations. The application of CFRP profiles is a promising alternative to steel in flexural-stiff stress-ribbon structural systems.

Author Contributions: Conceptualization, A.J.; methodology, A.J.; data curation, G.S.; investigation, G.S. and R.J.; software, R.J.; formal analysis, R.J. and V.G.; visualization, G.S. and R.J.; validation, A.J. and V.G.; writing—original draft preparation, G.S.; writing—reviewing and editing, V.G.; supervision, A.J.; resources, A.J.; project administration, R.J. All authors have read and agreed to the published version of the manuscript.

Funding: This project has received funding from the European Regional Development Fund (Project No. 01.2.2-LMT-K-718-03-0010) under grant agreement with the Research Council of Lithuania (LMTLT). The APC was funded by Vilnius Tech.

Institutional Review Board Statement: Not applicable.

Informed Consent Statement: Not applicable.

Data Availability Statement: Not applicable.

Conflicts of Interest: The authors declare no conflict of interest.

References

1. Strasky, J. *Stress Ribbon and Cable-Supported Pedestrian Bridges*; Thomas Telford: London, UK, 2005.
2. Goldack, A.; Schlaich, M.; Meiselbach, M. Stress ribbon bridges: Mechanics of the stress ribbon on the saddle. *ASCE J. Bridge Eng.* **2016**, *21*, 04015089. [[CrossRef](#)]
3. Tubino, F.; Pagnini, L.; Piccardo, G. Uncertainty propagation in the serviceability assessment of footbridges. *Struct. Infrastruct. Eng.* **2020**, *16*, 123–137. [[CrossRef](#)]
4. Romera, L.; Hernández, S.; Baldomir, A.; Nieto, F. Study of pedestrian comfort in a three span stress ribbon footbridge with carbon fibre cables. *WIT Trans. Built Environ.* **2020**, *196*, 139–152.
5. Xiao, X.; Xue, H.; Chen, B. Nonlinear model for the dynamic analysis of a time-dependent vehicle-cableway bridge system. *Appl. Math. Model.* **2021**, *90*, 1049–1068. [[CrossRef](#)]
6. Liu, Y.; Zwingmann, B.; Schlaich, M. Carbon fiber reinforced polymer for cable structures—A review. *Polymers* **2015**, *7*, 2078–2099. [[CrossRef](#)]
7. fib (The International Federation for Structural Concrete). *Guidelines for the Design of Footbridges*; fib: Lausanne, Switzerland, 2005.
8. Han, K.J.; Lim, N.H.; Ko, M.G.; Kim, K.D. Efficient assumption of design variables for stress ribbon footbridges. *KSCE J. Civ. Eng.* **2016**, *20*, 250–260. [[CrossRef](#)]
9. del Arco, C.D.; Aparicio, A.C.; Mari, A.R. Preliminary design of pre-stressed concrete stress ribbon bridges. *ASCE J. Bridge Eng.* **2001**, *6*, 234–241. [[CrossRef](#)]
10. Juozapaitis, A.; Norkus, A. Shape determining of loaded cable via total displacements. *Technol. Econ. Dev. Econ.* **2005**, *11*, 248–259. [[CrossRef](#)]
11. Scheer, J. *Failed Bridges: Case Studies, Causes and Consequences*; Ernst&Sohn Verlag: Berlin, Germany, 2010.
12. Radnić, J.; Matešan, D.; Buklijaš-Kobojević, D. Numerical model for analysis of stress-ribbon bridges. *Grđevinar* **2015**, *67*, 959–973.
13. Juozapaitis, A.; Vainiunas, P.; Kaklauskas, G. A new steel structural system of a suspension pedestrian bridge. *J. Constr. Steel Res.* **2006**, *62*, 1257–1263. [[CrossRef](#)]
14. Gholami, M.; Sam, A.R.M.; Yatim, J.M.; Tahir, M.M. A review on steel/CFRP strengthening systems focusing environmental performance. *Constr. Build. Mater.* **2013**, *47*, 301–310. [[CrossRef](#)]
15. Gholami, M.; Mohd Sam, A.R.; Marsono, A.K.; Tahir, M.M.; Faridmehr, I. Performance of steel beams strengthened with pultruded CFRP plate under various exposures. *Steel Compos. Struct.* **2016**, *20*, 999–1022. [[CrossRef](#)]
16. Arnautov, A.K.; Kulakov, V.; Andersons, J.; Gribniak, V.; Juozapaitis, A. Experimental investigation on stiffness and strength of single-lap z-pinned joints in a laminated CFRP stress-ribbon strip. *Balt. J. Road Bridge Eng.* **2016**, *11*, 120–126. [[CrossRef](#)]
17. Liu, Z.Q.; Luo, B.; Wang, Q.; Feng, B. Experimental and numerical investigation of the anti-debonding performance for novel CFRP-steel tube composite member under tension. *J. Build. Eng.* **2021**, *35*, 102004. [[CrossRef](#)]
18. Segal, E.M.; Rhode-Barbarigos, L.; Adriaenssens, S.; Coelho, R.D.F. Multi-objective optimization of polyester-rope and steel-rope suspended footbridges. *Eng. Struct.* **2015**, *99*, 559–567. [[CrossRef](#)]
19. Quaranta, G.; Demartino, C.; Xiao, Y. Experimental dynamic characterization of a new composite glulam-steel truss structure. *J. Build. Eng.* **2019**, *25*, 100773. [[CrossRef](#)]
20. Alaedini, S.; Kabir, M.Z.; Al-Mahaidi, R. Stability performance of thin-walled pultruded beams with geometric web-flange junction imperfections. *J. Build. Eng.* **2021**, *33*, 101549. [[CrossRef](#)]
21. Wadi, A.; Pettersson, L.; Karoumi, R. FEM simulation of a full-scale loading-to-failure test of a corrugated steel culvert. *Steel Compos. Struct.* **2018**, *27*, 217–227.
22. Votsis, R.A.; Stratford, T.J.; Chryssanthopoulos, M.K.; Tantele, E.A. Dynamic assessment of a FRP suspension footbridge through field testing and finite element modelling. *Steel Compos. Struct.* **2017**, *23*, 205–215. [[CrossRef](#)]
23. Bleicher, A.; Schlaich, M.; Fujino, Y.; Schauer, T. Model-based design and experimental validation of active vibration control for a stress ribbon bridge using pneumatic muscle actuators. *Eng. Struct.* **2011**, *33*, 2237–2247. [[CrossRef](#)]
24. Juozapaitis, A.; Merkevičius, T.; Daniūnas, A.; Kliukas, R.; Sandovič, G.; Lukoševičienė, O. Analysis of innovative two-span suspension bridges. *Balt. J. Road Bridge Eng.* **2015**, *10*, 269–275. [[CrossRef](#)]
25. Sandovic, G.; Juozapaitis, A.; Gribniak, V. Experimental and analytical investigation of deformations and stress distribution in steel bands of a two-span stress-ribbon pedestrian bridge. *Math. Probl. Eng.* **2017**, *2017*, 9324520. [[CrossRef](#)]
26. Juozapaitis, A.; Norkus, A. Determination of rational parameters for the advanced structure of a pedestrian suspension steel bridge. *Balt. J. Road Bridge Eng.* **2007**, *2*, 173–181.
27. Tong, Z.; Song, X.; Huang, Q. Deflection calculation method on GFRP-concrete-steel composite beam. *Steel Compos. Struct.* **2018**, *26*, 595–606.
28. Jakubovskis, R.; Kupliauskas, R.; Rimkus, A.; Gribniak, V. Application of FE approach to deformation analysis of RC elements under direct tension. *Struct. Eng. Mech.* **2018**, *68*, 345–358.
29. Cervenka, V.; Jendele, L.; Cervenka, J. *ATENA Program. Documentation, Part. 1: Theory*; Cervenka Consulting: Prague, Czechia, 2007.
30. Fiberline. *The Fiberline Design Manual*, 2nd ed.; Fiberline Composites: Middelfart, Denmark, 2003.
31. Röchling. *Durostone® Composite Profiles: Fibre Reinforced Plastics*; Röchling Industrial: Laupheim, Germany, 2017.